Applied Physics Letters

Direct electrical observation of plasma wave-related effects in GaN-based two-dimensional electron gases

Cite as: Appl. Phys. Lett. **105**, 173508 (2014); https://doi.org/10.1063/1.4900964
Submitted: 05 August 2014 . Accepted: 19 October 2014 . Published Online: 30 October 2014

Y. Zhao, W. Chen, W. Li, M. Zhu, Y. Yue, B. Song, J. Encomendero, B. Sensale-Rodriguez, H. Xing, and P. Fay

Direct electrical observation of plasma wave-related effects in GaN-based two-dimensional electron gases

Y. Zhao,[1] W. Chen,[1] W. Li,[1] M. Zhu,[1] Y. Yue,[1] B. Song,[1] J. Encomendero,[1]
B. Sensale-Rodriguez,[2] H. Xing,[1] and P. Fay[1,a)]
[1]*Department of Electrical Engineering, University of Notre Dame, Notre Dame, Indiana 46556, USA*
[2]*Department of Electrical and Computer Engineering, University of Utah, Salt Lake City, Utah 84112, USA*

(Received 5 August 2014; accepted 19 October 2014; published online 30 October 2014)

In this work, signatures of plasma waves in GaN-based high electron mobility transistors were observed by direct electrical measurement at room temperature. Periodic grating-gate device structures were fabricated and characterized by on-wafer G-band (140–220 GHz) s-parameter measurements as a function of gate bias voltage and device geometry. A physics-based equivalent circuit model was used to assist in interpreting the measured s-parameters. The kinetic inductance extracted from the measurement data matches well with theoretical predictions, consistent with direct observation of plasma wave-related effects in GaN-channel devices at room temperature. This observation of electrically significant room-temperature plasma-wave effects in GaN-channel devices may have implications for future millimeter-wave and THz device concepts and designs.
 [http://dx.doi.org/10.1063/1.4900964]

Applications of electromagnetic radiation in the millimeter-wave through terahertz region are potentially very attractive for advance functionalities such as remote sensing, spectroscopy, and ultra-wide bandwidth communications. However, in practice, it is difficult to obtain sufficient high-frequency performance with conventional electronic devices to practically implement THz electronic systems. This difficulty leads to the desire to explore alternative physical effects that can be exploited to enhance device performance. Plasma waves in 2-dimensional electron gases (2DEG)[1,2] are one such physical effect that has been reported to be a promising candidate for THz applications.[3] Previously, plasma waves have been observed at room temperature in GaAs/AlGaAs and InGaAs/InAlAs heterostructures [e.g., Refs. 4–7]. In contrast to As-based heterostructure device structures, III-N heterostructures are potentially advantageous for novel device concepts due to their large bandgap and much higher 2DEG carrier concentration that arises from polarization in these materials. However, due to the modest mobility of GaN-based 2DEGs, plasma-wave effects have previously only observed by quasi-optical measurements of THz emission and detection [see, e.g., Refs. 8 and 9] and low-temperature optical absorption and transmission [see, e.g., Ref. 10]. While these prior reports provide evidence for the formation of plasma waves in GaN-based 2DEGs, they do not provide a direct measure of the electrical significance of the plasma waves on device operation, and thus provide limited guidance on how these effects might be exploited for novel all-electronic device concepts. To enhance the observability of the plasma-wave effects and obtain the electrical signatures of this phenomenon, periodic grating-gate structures were used. In these structures, standing waves generated within the grating-gate high electron mobility transistors (HEMTs) provide more robust and unambiguous interpretation of the measurement results. On-wafer s-parameter measurements from 140–220 GHz (G-band) were obtained as a function of both device bias conditions and device geometry, and a physics-based equivalent circuit model has been developed to assist in the interpretation of the measured millimeter-wave s-parameters. The fundamental difference between the model developed here and conventional HEMT models is its distributed nature with the inclusion of the distributed kinetic inductance along the 2DEG, which originates from the collective carrier motion. A preliminary evaluation of these data was reported in Ref. 11; in this work, we provide a thorough analysis and demonstrate that good agreement between the extracted kinetic inductance and the theoretical predictions has been obtained, providing clear indication of the existence of plasma wave–related phenomena in the GaN 2DEG within the devices, as well as a direct indication of their significance for device applications.

Figure 1(a) shows a schematic diagram of the grating-gate HEMT device structure and the heterostructure used in

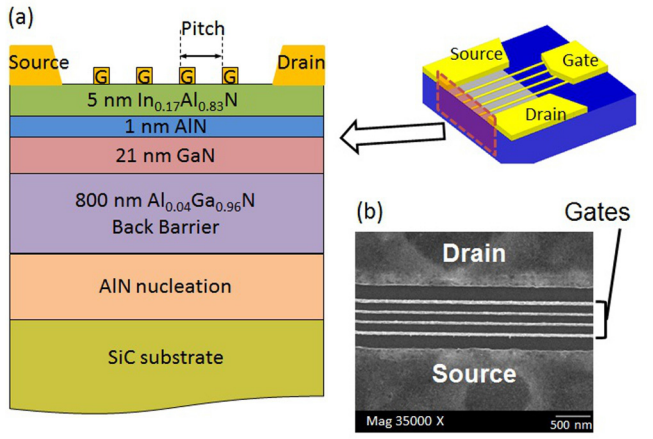

FIG. 1. (a) Cross-sectional schematic diagram of a grating-gate HEMT and the associated heterostructure; (b) SEM image of a typical grating-gate HEMT showing placement of the 4-electrode grating gate within the source-drain spacing.

a)E-mail: pfay@nd.edu

this work. For most of the data reported here, the devices included four gate electrodes connected to a common gate pad within each device, as shown in Fig. 1. The InAlN/AlN/GaN/AlGaN heterostructure was grown by metallorganic chemical vapor deposition (MOCVD) with an as-grown sheet resistance of 283 Ω/sq. Device processing was based on a conventional gate-last GaN HEMT process, which included Cl_2-based reactive ion etching for mesa isolation, evaporation of Ti/Al/Ni/Au for Ohmic contact followed by rapid thermal annealing in a N_2 ambient, and electron beam lithography (EBL) for defining the grating gate pattern followed by liftoff of 20 nm thick evaporated Ni to form the gate electrodes. To improve the alignment accuracy between the gate and ohmic metallization and to reduce the edge roughness of the source and drain metallization, EBL was also used to define the ohmic pattern near the channel, while the bulk of the contact pads was defined by optical lithography to reduce EBL write times. The devices were left unpassivated to minimize parasitic capacitance. To assist in s-parameter calibration and de-embedding, calibration structures were fabricated on-wafer alongside the devices to de-embed the pad parasitics.

For the study reported here, grating-gate HEMTs with three different gate grating pitches from (110–170 nm) were fabricated, as well as single-gate devices. Figure 1(b) shows a scanning electron microscope (SEM) image of a typical fabricated grating-gate device with a gate pitch of 150 nm. The average individual gate length is 36 nm, and the channel width is 13.9 μm. As can be seen, good alignment of the gate grating within the source-drain spacing and smooth edges of the ohmic pattern have been achieved.

To facilitate interpretation of the measured millimeter-wave HEMT characteristics, a R-L-C-G transmission line model was used to model the behavior of the plasma waves in the 2DEGs.[3,4,12] Equation (1) shows the relationship between R-L-C-G equivalent circuit parameters and the physical properties of the 2DEG[3]

$$R = \frac{1}{q\mu n_s W}, \quad L = \frac{m^*}{q^2 n_s W}, \quad C = c_o W, \quad G = g_o W, \quad (1)$$

where R, L, C, and G are the distributed resistance, inductance, capacitance, and conductance, of the equivalent transmission line, n_s is the carrier concentration of the 2DEGs (and is a function of gate bias voltage), W is the channel width, μ is carrier mobility, m* is the electron effective mass, g_o is the gate conductance per area, and c_o is the gate capacitance per area. From Eq. (1), it can be seen that the R, G, and C transmission line parameters have conventional interpretations as the distributed channel resistance, gate-to-channel capacitance, and gate-to-channel conductance (i.e., gate leakage), respectively. Plasma-wave behavior appears in the inductive (L) term, which is neglected in conventional high-frequency HEMT models; this L represents the (bias dependent) kinetic inductance associated with the plasma wave propagation. Transmission lines of this type can also be described in terms of the characteristic impedance ($Z_o = \sqrt{(R + j\omega L)/G + j\omega C}$) and the complex propagation constant ($\gamma = \sqrt{(R + j\omega L)(G + j\omega C)}$).

Because the gate voltage modulates n_s in the channel region under the gate electrodes, Eq. (1) indicates that the wave propagation in the 2DEGs should be different under the gates and in the inter-gate spaces. Consequently, a useful electrical analogy to the grating-gate HEMT is as illustrated in Figs. 2(a) and 2(b). The equivalent circuit—which consists of a cascade of multiple transmission lines in series—is shown in Figure 2(a). In Fig. 2(a), the diameter of the cylinders is intended to convey the modulation in transmission line Z_o as a function of position along the channel. Figure 2(b) shows the detailed R-L-C-G transmission line model; in this model, the R-L-C-G parameters are a function of position along the channel, in accordance with Eq. (1). The periodic grating-gate structure induces periodic wave propagation characteristics along the channel, leading to an equivalent circuit that is analogous to a stepped-impedance filter between source and drain electrodes. In such a circuit, the frequency response of the filter can be tuned by the applied gate voltage, through the variation in gate capacitance, c_o, and n_s.

The model shown in Figs. 2(a) and 2(b) corresponds to the intrinsic device; in practice, the actual device structure will also have wiring inductance on each lead, as well as finite resistance from the contacts and thin gate electrode metallization. To account for these effects, a series resistance associated with the thin Ni gate metal was added to the model, and series inductances L_s and L_d were used to account for the parasitic wiring inductance from the on-wafer probe pads.

To analyze the validity of the model and extract the model parameters, millimeter-wave performance of the fabricated gating-grate HEMTs was measured. A vector network analyzer was used to obtain the s-parameters of the devices as a function of device geometry (three different gate grating pitches plus single-gate devices), bias conditions, and frequency. To facilitate on-wafer probing,

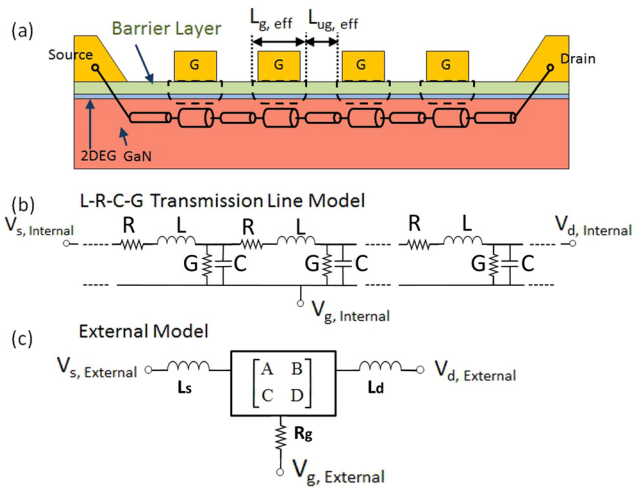

FIG. 2. (a) Electrical transmission line analogy for analyzing the plasma-wave grating-gate HEMT. The cylinder diameter illustrates conceptually the characteristic impedance of the transmission line sections, arising from the variation in c_o and n_s along the channel. The dashed lines show the gate depletion regions schematically. (b) R-L-C-G transmission line equivalent circuit of the stepped-impedance filter model used to model the grating-gate GaN HEMTs; the transmission line parameters vary with position along the channel due to gate-induced modulation of c_o and n_s. (c) Electrical model showing inclusion of extrinsic gate resistance and source and drain inductances within the model; the intrinsic device is treated in matrix form with an ABCD formulation.

coplanar ground-signal-ground probes with 100 μm pitch were used. The network analyzer was calibrated using off-wafer standards using a line-reflect-reflect-match (LRRM) calibration, followed by on-wafer calibration using the calibration structures fabricated alongside the devices as a second calibration tier. For the measurements shown here, the gate was connected to port 1, the drain to port 2, and the source was grounded, resulting in common-source s-parameters. These measured common-source s-parameters were mathematically converted to common-gate s-parameters for easy comparison with the equivalent stepped-impedance filter (for which the gate is common and the inputs and outputs are at the source and drain, respectively) shown in Figure 2. The s-parameters were measured over a range of gate voltages from pinchoff into accumulation of the channel. For all measurements, the drain-source bias voltage was set to zero in order to eliminate channel concentration modulation from the drain bias.

Figure 3 shows the measured DC transfer characteristics and gate capacitance-voltage (C-V) characteristics of a typical 150 nm-pitch grating-gate HEMT. As can be seen, the on/off ratio of drain current exceeds 10^8 with clear pinchoff. Low gate leakage—which was measured at less than 10^{-8} A/mm at the on-state—was obtained. Compared with conventional devices reported previously on similar heterostructures,[13] the DC performance is compromised because of the comparatively high as-grown sheet resistance (in Ref. 13, re-grown n+ ohmic contact layers in close proximity to the device were used to reduce access resistance), and the large on-resistance and low transconductance is caused by the long "effective" gate length originating from having 4 gates in series in the grating-gate devices reported here.

To compare the model illustrated in Fig. 2 to the actual device behavior, on-wafer s-parameters were measured as a function of applied gate voltage (from −0.95 to 1 V in 0.15 V steps), gate geometry (single gate and grating gates with 110, 150, and 170 nm pitches), and frequency (from 140 to 220 GHz). From this measured data, the equivalent circuit model parameters were extracted using least-squares fitting. To reduce the number of parameters in the fitting, the measured C-V was used to fix the capacitance c_o in the gated regions, while g_o in both gated and ungated regions was set to zero due to the low gate leakage measured in these devices. Thus, only the R and L in both the gated regions were allowed to vary with gate bias in the least-squares fitting, while parameters associated with the ungated regions were required to remain independent of the gate bias.

In this way, a single set of self-consistent equivalent circuit parameters were extracted from four devices. The four devices include three grating-gate HEMTs with 110, 150, and 170 nm pitches, respectively, and a single-gate HEMT. Figure 4 shows the magnitude and phase of the measured common-gate transmission s-parameters and the equivalent circuit model response for the common-gate transmission parameter s_{12} at two representative gate-source voltage (V_{gs}) values (−0.05 V and 1 V; other values were used in the fitting but are quite similar and are not shown). As can be seen, for all the gate geometries (devices with a single gate or four gate fingers with 110 nm, 130 nm, and 170 nm gate pitches), the results from the equivalent circuit model (solid lines) fit the experimental data (circle markers) reasonably well over the full frequency range. The relatively weak frequency dependence observed indicates that the plasma waves are heavily damped under these experimental conditions, consistent with theoretical expectations. The L_2 error of the circuit model response compared with the experimental data is shown in Figure 5. As can be seen, the L_2 error of the magnitude and phase is less than 0.4 dB and 4°, respectively, over the full frequency range and for V_{gs} from −0.95 to 1 V. The error increased at higher negative bias since a more complicated charge density model is needed for the higher electric field as the channel depletes.

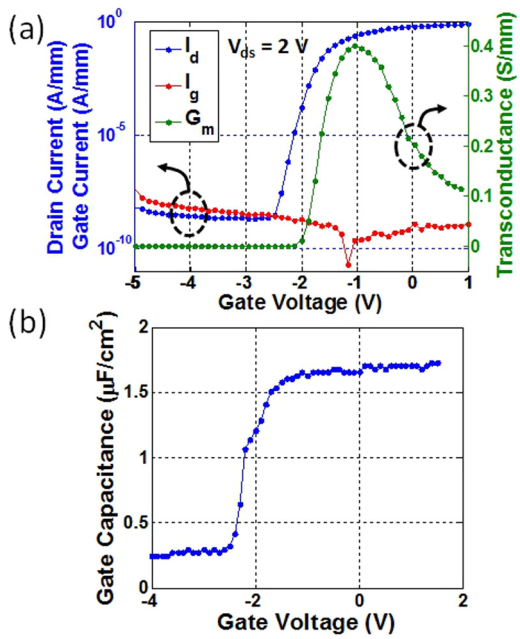

FIG. 3. Measured (a) common-source transfer characteristics and gate leakage, and (b) measured gate C-V characteristic for a typical grating gate HEMT of 150 nm pitch.

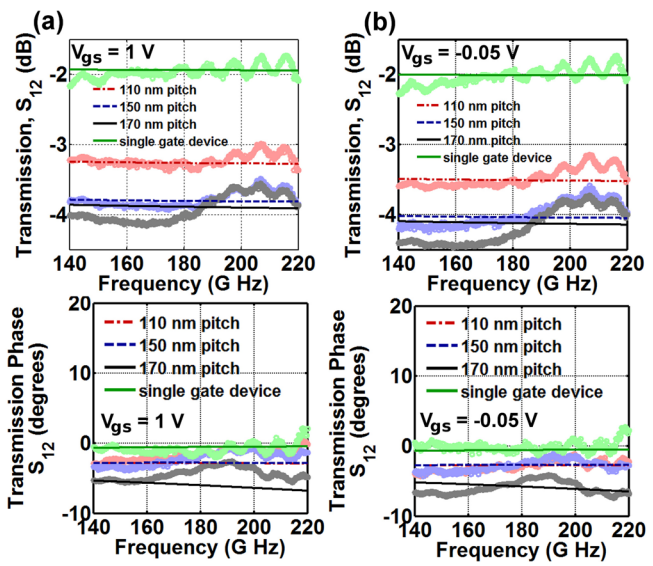

FIG. 4. Magnitude and phase of the common-gate transmission (s_{12}) for grating-gate GaN HEMTs at two selected fixed gate biases: (a) $V_{gs} = 1$ V and (b) $V_{gs} = -0.05$ V. Lines are the calculated results from the filter equivalent circuit model, circles show on-wafer measurement results.

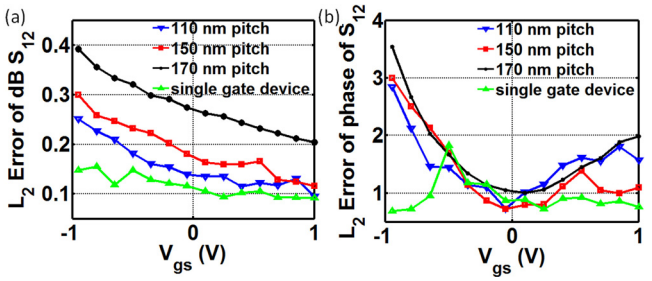

FIG. 5. L_2 error of the (a) magnitude and (b) phase of the equivalent circuit model response compared with the experimental data. Magnitude errors of less than 0.4 dB and phase errors below 4° have been obtained.

The gate bias dependence of the measured s_{12} (magnitude and phase) as a function of gate bias and gate pitch for two typical devices is shown in Fig. 6. As can be seen, the results from the equivalent circuit model effectively track the trend with applied bias, and the deviation between the equivalent circuit results and the experimental data is less than 0.5 dB and 8° over the full range of frequencies and gate pitches evaluated here. At a typical bias of $V_{gs} = -0.05$ V, the transmission line parameters for the gated sections are $R = 51.3$ MΩ/m, $L = 1.97$ μH/m, and $C = 0.23$ μF/m, indicating that the kinetic inductance term contributes approximately 5% to the impedance magnitude and approximately 3° to the phase, despite the significant plasma wave damping. In addition, modeling the device without including kinetic inductance (not shown) resulted in appreciably larger L_2 errors, and in particular was not able to accurately capture the observed gate bias dependence.

Figure 7 shows the extracted kinetic inductance compared with theoretical predictions by combining Eq. (1) with the equivalent circuit shown in Fig. 2 obtained from the full measurement array (frequency from 140–220 GHz with gate biases from −0.95 V to +1 V and gate pitches of 110 nm, 150 nm, and 170 nm as well as single-gate devices). Square markers show the kinetic inductance extracted by using four

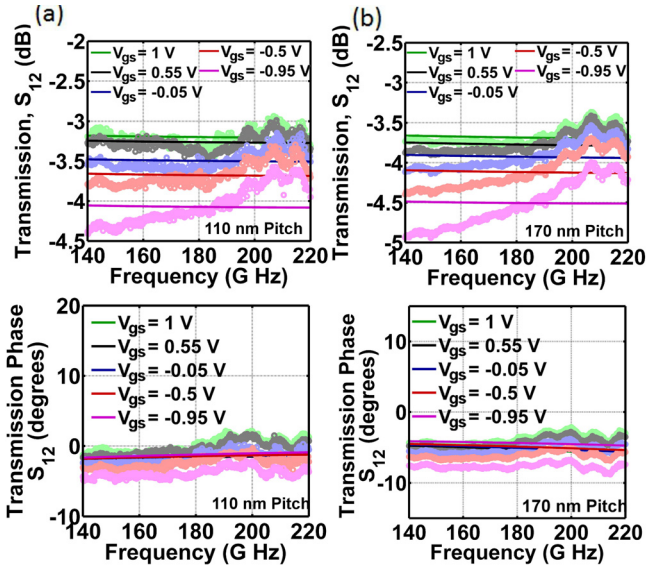

FIG. 6. Common-gate transmission (s_{12}) for grating-gate GaN HEMTs as a function of gate bias for two selected gate pitches: (a) 110 nm pitch and (b) 170 nm pitch. Solid lines are the calculated results from the filter equivalent circuit model, circles show measurement results.

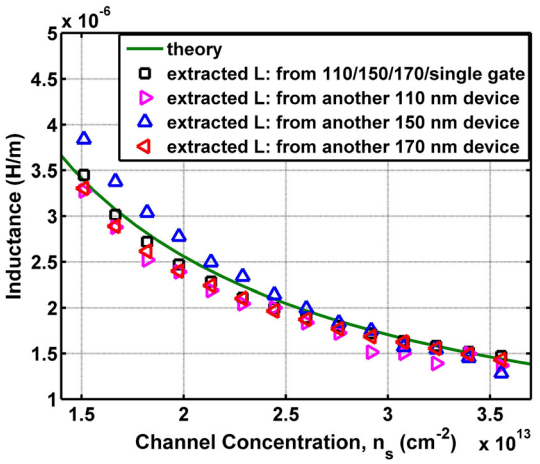

FIG. 7. Extracted kinetic inductance and theoretical projection vs. n_s. The inductance extracted jointly from 4 devices (grating gate pitches of 110, 150, and 170 nm as well as a single-gate device) is shown with the square markers, and the results of extracting the inductance from individual grating-gate GaN HEMTs across the sample is shown with triangles. The solid line shows the theoretical prediction based on Eq. (1) in conjunction with the equivalent circuit shown in Fig. 2.

devices in combination (all four gate geometries were used simultaneously in the parameter extraction), while triangles show the results extracted from single devices (only data from a single device was used for the parameter extraction). As can be seen, excellent agreement between the extracted kinetic inductance and the theoretical prediction in Eq. (1) is obtained over all devices and the full range of bias conditions and channel charge densities. The excellent agreement with the theory—and in particular the existence of the channel-charge dependent channel inductance—is characteristic of plasma waves. The value of the kinetic inductance (ranging from 1.5 μH/m to 3.5 μH/m) is small enough to be negligible for conventional microwave-frequency device operation, but at submillimeter-wave and THz frequencies can contribute significantly to device behavior.

The kinetic inductance signature associated with plasma waves in GaN-based grating-gate HEMTs has been observed by direct millimeter-wave electrical measurement at room temperature. A physics-based transmission line equivalent circuit model analogous to a stepped-impedance distributed filter was used to interpret the measured s-parameters. The extracted kinetic inductance matches well with the theoretical model over the full range of the measured bias conditions, indicating the significance of the kinetic inductance term in evaluating the 2DEG electrical characteristics at millimeter-wave (140–220 GHz) frequencies. This observation of electrically significant room-temperature plasma-wave effects in GaN-channel devices may have implications for future millimeter-wave and THz device concepts and designs.

This work was supported by the Office of Naval Research, N00014-11-1-0721, Devices and Architectures for THz Electronics MURI, Paul Maki program manager.

[1]M. Dyakonov and M. S. Shur, Phys. Rev. Lett. **71**, 2465 (1993).
[2]M. Dyakonov and M. S. Shur, IEEE Trans. Electron Devices **43**, 380 (1996).

[3]B. Sensale-Rodriguez, L. Liu, P. Fay, D. Jena, and H. Xing, IEEE Trans. Terahertz Sci. Technol. **3**, 200 (2013).
[4]P. J. Burke, I. B. Spielman, J. P. Eisenstein, L. N. Pfeiffer, and K. W. West, Appl. Phys. Lett. **76**, 745 (2000).
[5]A. El Fatimy, F. Teppe, N. Dyakonova, W. Knap, D. Seliuta, and G. Valušis, Appl. Phys. Lett. **89**, 131926 (2006).
[6]F. Teppe, W. Knap, D. Veksler, M. S. Shur, A. P. Dmitriev, V. Yu. Kachorovskii, and S. Rumyantsev, Appl. Phys. Lett. **87**, 052107 (2005).
[7]X. G. Peralta, S. J. Allen, M. C. Wanke, N. E. Harff, J. A. Simmons, M. P. Lilly, J. L. Reno, P. J. Burke, and J. P. Eisenstein, Appl. Phys. Lett. **81**, 1627 (2002).
[8]T. Tanigawa, T. Onishi, S. Takigawa, and T. Otsuji, in Proceedings of IEEE Device Research Conference, 2010.
[9]A. El Fatimy, S. Boubanga Tombet, F. Teppe, W. Knap, D. B. Veksler, S. Rumyantsev, M. S. Shur, N. Pala, R. Gaska, Q. Fareed, X. Hu, D. Seliuta, G. Valušis, C. Gaquiere, D. Theron, and A. Cappy, Electron. Lett. **42**, 1342 (2006).
[10]A. V. Muravjov, D. B. Veksler, V. V. Popov, O. V. Polischuk, N. Pala, X. Hu, R. Gaska, H. Saxena, R. E. Peale, and M. S. Shur, Appl. Phys. Lett. **96**, 042105 (2010).
[11]Y. Zhao, W. Chen, M. Zhu, Y. Yue, B. Song, J. Encomendero, B. Sensale-Rodriguez, H. Xing, and P. Fay, in *Proceedings of International Symposium on Compound Semiconductors* (2014), p. Th-A2-4.
[12]I. Khmyrova and Y. Seijyou, Appl. Phys. Lett. **91**, 143515 (2007).
[13]M. Schuette, A. Ketterson, B. Song, E. Beam, T. Chou, M. Pilla, H. Tserng, X. Gao, S. Guo, P. Fay, H. Xing, and P. Saunier, IEEE Electron Device Lett. **34**, 741 (2013).